J. Fluid Mech. (2005), *vol.* 524, *pp.* 229–248. © 2005 Cambridge University Press
DOI: 10.1017/S0022112004002319 Printed in the United Kingdom

Orthogonal wavelet multi-resolution analysis of a turbulent cylinder wake

By AKIRA RINOSHIKA[1]† AND YU ZHOU[2]‡

[1]Department of Mechanical Systems Engineering, Yamagata University, 4-3-16 Jonan, Yonezawa-shi, Yamagata 992-8510, Japan

[2]Department of Mechanical Engineering, The Hong Kong Polytechnic University, Hung Hom, Kowloon, Hong Kong

(Received 18 March 2003 and in revised form 10 September 2004)

Previous studies of the organized motion mostly focused on large-scale structures; investigations of other scales have been relatively scarce because of the difficulty of extracting the structures of these scales using conventional vortex-detection techniques. A wavelet multi-resolution technique based on an orthogonal wavelet transform has been applied to analysing the velocity data simultaneously obtained in two orthogonal planes in the turbulent near-wake of a circular cylinder. Using this technique, the flow is decomposed into a number of wavelet components based on their characteristic or central frequencies. The flow structure of each wavelet component is examined in terms of sectional streamlines and vorticity contours. The wavelet component at a central frequency of f_0, the same as the vortex-shedding frequency, exhibits the characteristics of the Kármán vortices, thus providing a validation of the analysis technique. The spanwise vorticity contours of the wavelet component at f_0 display a secondary spanwise structure near the saddle point, whose vorticity is opposite-signed to that of the Kármán vortices. This structure is observed for the first time and its occurrence is consistent with the streamwise decay in the vorticity strength of the spanwise structures. Two-point velocity correlations of wavelet components in the lateral and spanwise directions and the wavelet auto-correlation function indicate that the wavelet components of f_0 and $2f_0$ are relatively large-scale and organized, displaying considerable two-dimensionality. The component of $4f_0$ is significantly less organized and highly three-dimensional, as indicated by much smaller spanwise correlation coefficients. The components at frequencies of $8f_0$ and higher have virtually zero correlation coefficients.

1. Introduction

The turbulent near wake of a circular cylinder is characterized by a high degree of organization, which makes it suitable for studying turbulent structures in terms of their organized aspects and clarifying their role in the transport process. In this flow, turbulent structures consist of a wide range of scales, including large-scale spanwise structures and relatively small-scale structures such as the secondary vortices (Wei & Smith 1986), Kelvin–Helmholtz vortices (Lin, Vorobieff & Rockwell 1996) and longitudinal rib-like structures (e.g. Hussain & Hayakawa 1987). Our understanding

† Also known as Hui Li.
‡ Author to whom correspondence should be addressed: mmyzhou@polyu.edu.hk.

https://doi.org/10.1017/S0022112004002319 Published online by Cambridge University Press

of large-scale spanwise structures has been greatly improved in the last two decades or so. This is partly attributed to the successful development of various schemes for educing these structures from turbulent flows, such as the phase-averaging technique (e.g. Cantwell & Coles 1983; Kiya & Matsumura 1988; Zhou, Zhang & Yiu 2002), the vorticity-based technique (e.g. Hussain & Hayakawa 1987; Zhou & Antonia 1993), the pattern-recognition technique (Ferre & Giralt 1989) and the scheme based on critical points (Zhou & Antonia 1994*a*). In contrast, there is a lack of reliable techniques that could educe the turbulent structures of scales other than the large-scale vortices from measured or numerical data. Our knowledge of these structures is mostly obtained from flow visualization and DNS data (e.g. Wei & Smith 1986; Williamson 1996*a*; Wu *et al.* 1996). Brede, Eckelmann & Rockwell (1996), Lin *et al.* (1996) and Chyu & Rockwell (1996) characterized the patterns of instantaneous streamwise vorticity concentrations in the transitional and turbulent near wakes. Nevertheless, many aspects of these structures, including their role in the momentum transport and relation with the large-scale structures, have yet to be completely understood.

In the past decade, there has been a growing interest in applying the wavelet technique to the analysis of turbulent flow data (e.g. Farge 1992). This technique allows time- (or spatial-) and frequency-domain analyses to be combined and decomposes the flow structures based on frequencies or scales. The wavelet analysis may be roughly classified into continuous and discrete wavelet transforms. The former is performed in a smooth continuous fashion, i.e. using the continuous wavelet function, while the latter is carried out in discrete steps, i.e. using the discrete orthogonal wavelet basis.

The continuous wavelet transform can be used to provide continuous time–frequency identification of eddy structures. The technique has been widely used to analyse hot-wire signals, for example, by Argoul *et al.* (1989) to investigate the wind-tunnel turbulence, Liandrat & Moret-Bailly (1990) and De Souza *et al.* (1999) in a boundary layer, Li & Nozaki (1995) in a turbulent jet, Higuchi, Lewalle & Crane (1994) in a turbulent wake, Li (1998) and Bonnet *et al.* (1998) in turbulent shear flows.

In contrast, the discrete wavelet transform is characterized by an orthogonal projection on a minimal number of independent modes, allowing quantitative information to be extracted. This transform is further readily invertible, enabling the original data to be reconstructed uniquely for any chosen wavelet basis function from the wavelet coefficients of its inverse transform. This technique has been applied to analyse the turbulent structures of various scales as well as coherent structures (Meneveau 1991; Farge, Schneider & Kevlahan 1999; Mouri *et al.* 1999). Mallat (1989) developed an orthogonal wavelet multi-resolution technique based on the discrete wavelet transform. This technique may provide a simple hierarchical framework to represent a signal, which allows an event in the signal to be decomposed into a number of events with fine details. The technique is further potentially capable of decomposing and characterizing quantitatively, other than coherent and incoherent structures, the turbulent structures based on their characteristic frequencies (or scales) in the time (or spatial) domain, which has not been given much attention in the literature.

This work applies an orthogonal wavelet multi-resolution technique for the analysis of turbulent velocity data in order to characterize the turbulent structures in both Fourier and physical spaces. The technique is used to analyse experimental data obtained in the turbulent near wake of a circular cylinder. The investigation aims to decompose turbulent structures into a number of wavelet components based on their wavelet levels or central frequencies, which are linked to the turbulent structure scales. Based on the decomposed wavelet components, the turbulent structures of various scales are examined in detail, including their vortcity contours and streamline patterns,

https://doi.org/10.1017/S0022112004002319 Published online by Cambridge University Press

probability density function, three-dimensional aspects, autocorrelation functions, two-point correlation coefficients, and interrelationship between different scales.

2. Orthogonal wavelet multi-resolution analysis

Orthogonal wavelet transform and multi-resolution analysis are discussed in detail in Mallat (1989), for example, and are therefore discussed only briefly in this section.

One-dimensional discrete wavelet transform is a linear and orthogonal transform, defined in matrix form by

$$\boldsymbol{S} = \boldsymbol{W}\boldsymbol{V}, \tag{1}$$

where $\boldsymbol{V}$ is a one-dimensional data matrix, namely,

$$\boldsymbol{V} = [v_1 \quad v_2 \quad \ldots \quad v_N]^T, \tag{2}$$

$\boldsymbol{S}$ and $\boldsymbol{W}$ are called the discrete wavelet coefficient (or spectrum) matrix and the analysing wavelet matrix of $\boldsymbol{V}$, respectively. The superscript T in (2) denotes a transposed matrix. $\boldsymbol{W}$ is orthogonal and satisfies $\boldsymbol{W}^T\boldsymbol{W} = \boldsymbol{I}$, where $\boldsymbol{I}$ is a unit matrix. $\boldsymbol{W}$ is usually constructed based on a cascade algorithm of an orthogonal wavelet basis function. In the present study, the Daubechies wavelet basis with an order of 20 (Daubechies 1992) is used since the wavelet basis of a higher order has good frequency localization, which in turn increases the energy compaction.

Both the analysing wavelet matrix and wavelet basis are orthogonal, implying that the discrete wavelet transform has the inverse transform. We simply reverse the procedure, starting with the smallest level of the hierarchy and working from right to left, and the inverse discrete wavelet transform is given by

$$\boldsymbol{V} = \boldsymbol{W}^T\boldsymbol{S}. \tag{3}$$

The discrete wavelet coefficient may be interpreted as the relative local contribution of various scales to the original data. In order to decompose the data into the grouped frequency components, the inverse wavelet transform is applied to the discrete wavelet coefficients at each grouped frequency. This decomposition method is called the wavelet multi-resolution analysis. Hence, (3) can be rewritten as

$$\boldsymbol{V} = \sum_{i=1}^{n} \boldsymbol{W}^T\boldsymbol{S}_i. \tag{4}$$

On the right-hand side of (4), the first term $\boldsymbol{W}^T\boldsymbol{S}_1$ and the last term $\boldsymbol{W}^T\boldsymbol{S}_n$ represent the wavelet components at wavelet level 1 (the lowest frequency) and level n (the highest frequency).

If the data set is a two-dimensional array, the two-dimensional discrete wavelet transform of data $\boldsymbol{V}$ is given by

$$\boldsymbol{S} = \boldsymbol{W}\boldsymbol{V}\boldsymbol{W}^T, \tag{5}$$

which amounts to performing a one-dimensional discrete wavelet transform in two directions. Thus, its inverse discrete wavelet transform is

$$\boldsymbol{V} = \boldsymbol{W}^T\boldsymbol{S}\boldsymbol{W}. \tag{6}$$

Similarly to (4), the two-dimensional wavelet multi-resolution analysis is given by

$$\boldsymbol{V} = \sum_{i=1}^{n} \boldsymbol{W}^T\boldsymbol{S}_i\boldsymbol{W}. \tag{7}$$

https://doi.org/10.1017/S0022112004002319 Published online by Cambridge University Press

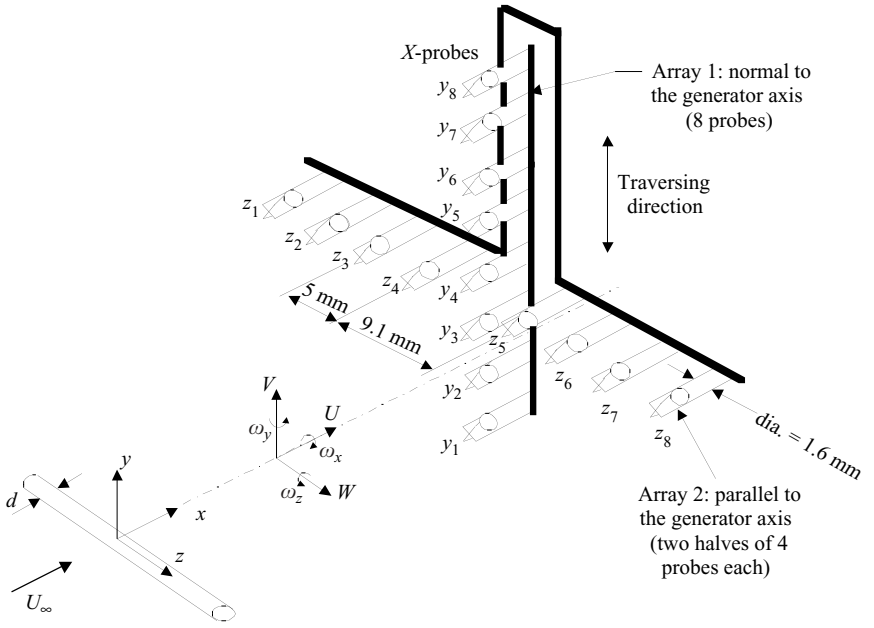


FIGURE 1. Experimental set-up.

It is worth remarking that, compared with conventional band-pass filtering techniques, the wavelet components of the discrete wavelet transform are orthogonal to, and hence independent of, each other and do not contain redundant information. This advantage makes the interpretation of the phenomena more reliable (Mouri *et al.* 1999).

3. Experimental data and orthogonal wavelet decomposition

The technique described in § 2 is applied to analyse two-dimensional velocity data obtained using cross-wires. Experimental details were described in Zhou & Antonia (1994*b*). Figure 1 shows the experimental arrangement. Briefly, a circular cylinder ($d = 12.5$ mm) was used to generate a turbulent wake. Measurements were conducted at $x/d = 20$ (x is the streamwise distance downstream of the cylinder) and a constant free-stream velocity ($U_\infty = 6.7\,\mathrm{m\,s^{-1}}$). The corresponding Reynolds number Re ($\equiv U_\infty d/\nu$) was 5600. The Kolmogorov length scale at this x/d was estimated to be about 0.16 mm. Two orthogonal arrays, each of eight cross-wires, were used. Eight cross-wires were aligned in the (x, y)-plane, i.e. the plane of mean shear, and eight in the (x, z)-plane, which is parallel to both the cylinder axis and the streamwise direction. The sixteen cross-wires allow velocity fluctuations u and v in the (x, y)-plane and u and w in the (x, z)-plane to be obtained simultaneously. The nominal spacing between cross-wires was about 5 mm, except for a relatively large gap (9.2 mm) between the fourth and fifth cross-wires in the (x, z)-plane. The arrays were attached to separate traversing mechanisms and could be moved independently of each other. The eight cross-wires in the (x, y)-plane were fixed with the bottom cross-wire positioned at $y/d \approx -0.3$; the eight cross-wires in the (x, z)-plane were located at $y/d \approx 0.2$ and 0.68. The physical blockage caused by these arrays, cable and supports was estimated to be about 3%. The interference to the flow due to the two arrays was negligible. Wollaston (Pt–10% Rh) wires, 5 μm in diameter and about

https://doi.org/10.1017/S0022112004002319 Published online by Cambridge University Press

1 mm in working length, were operated with constant-temperature circuits. Signals from the circuits were offset, amplified and then digitized using two 16-channel (12 bit) A/D boards and two personal computers at a sampling frequency of $f_s = 3.5$ kHz per channel (the cut-off frequency was 1.6 kHz). Data acquisition by the two computers was synchronized using a common external trigger pulse. The sampling duration was about 38 s.

The measured instantaneous velocity V_k can be written as

$$V_k = \overline{V}_k + v_k, \tag{8}$$

where the overbar denotes the time-averaging operation and v_k is the fluctuation component, the subscript $k = 1$, 2 and 3 represents the velocity components in the x-, y- and z-direction, respectively. Using the wavelet multi-resolution technique, v_k is decomposed into a number of orthogonal wavelet components based on the central frequencies/wavelet levels, which may be linked to the turbulent structure scales. Each wavelet component represents the turbulent structures of a certain range of frequencies (i.e. a non-zero frequency bandwidth) so that the information of any scales contained in the original data will not be lost because of a limited number of wavelet levels. In line with (8), v_k may be written as

$$v_k = \sum_{i=1}^{N} v_{k,i}, \tag{9}$$

where $v_{k,i}$ is the wavelet component of v_k at the ith wavelet level.

Since measurements indicate that $\overline{V} \approx 0$ and $\overline{W} \approx 0$, the instantaneous wavelet components of velocity in the x-, y- and z-directions, respectively, are written as

$$\left.\begin{aligned} U_i &= \overline{U} + u_i, \\ V_i &\approx v_i, \\ W_i &\approx w_i. \end{aligned}\right\} \tag{10}$$

Vorticity may be approximated based on velocity data using the central difference approximation (Hussain & Hayakawa 1987). Thus, the eight cross-wires in each plane may produce vorticity data at each of the seven midpoints between adjacent cross-wires. The wavelet components of spanwise and transverse vorticity at the ith wavelet level in the (x, y)- and (x, z)-plane, respectively, may be approximated by

$$\omega_{zi} = \frac{\partial V_i}{\partial x} - \frac{\partial U_i}{\partial y} = \frac{\partial v_i}{\partial x} - \frac{\partial (\overline{U} + u_i)}{\partial y} \approx \frac{\Delta v_i}{\Delta x} - \frac{\Delta (\overline{U} + u_i)}{\Delta y}, \tag{11}$$

and

$$\omega_{yi} = \frac{\partial U_i}{\partial z} - \frac{\partial W_i}{\partial x} = \frac{\partial u_i}{\partial z} - \frac{\partial w_i}{\partial x} \approx \frac{\Delta u_i}{\Delta z} - \frac{\Delta w_i}{\Delta x}, \tag{12}$$

where Δy or Δz (≈ 5.0 mm) is the spacing between two cross-wires; $\Delta x = -\overline{U}\Delta t = -\overline{U}/f_s$. Note that since vorticity is indirectly calculated from velocity signals using the central difference approximation, spacing between cross-wires may degrade the spatial resolution of vorticity. However, the approach should be adequate for describing and providing at least useful qualitative information on the relatively large-scale and intermediate-scale vorticity field (Zhang, Zhou & Antonia 2000). For simplicity, the average vortex convection velocity $U_c = 0.87U_\infty$ of large-scale vortical structures on the vortex path (Zhou & Antonia 1992) was used to calculate Δx. Vorticity contours

https://doi.org/10.1017/S0022112004002319 Published online by Cambridge University Press

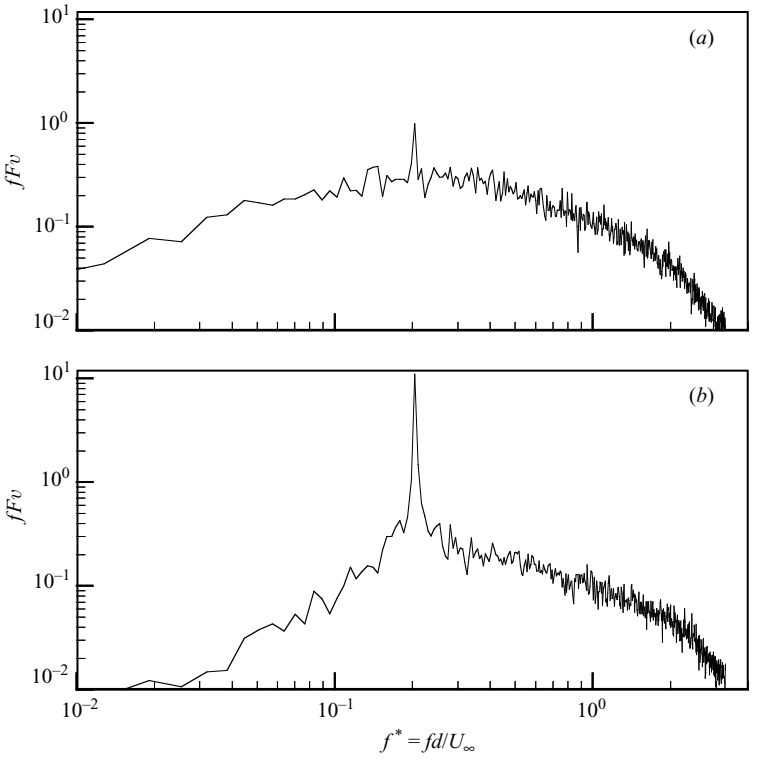


FIGURE 2. Spectra of the u- and v-signals at $y/d \approx 0.7$.

and r.m.s. values thus obtained showed no appreciable difference from those obtained using the local mean velocity.

4. Central frequencies and their bandwidths of wavelet components

A fundamental central frequency of turbulent structures has to be determined for the wavelet multi-resolution analysis. This frequency is presently specified at the averaging frequency, f_0, of Kármán vortices. Figure 2 shows the power spectra of the u and v signals at $y/d \approx 0.7$, which is approximately on the vortex path. The power spectral density functions F_u and F_v are weighted by frequency f to indicate the energy distribution with f. Both fFu and fFv show a pronounced peak at $f_0^* = f_0 d/U_\infty \approx 0.2$, the well-known vortex-shedding frequency or Strouhal number in a circular cylinder wake. Once the fundamental central frequency is determined, the v-signal at $y/d \approx 0.7$ is decomposed using the wavelet multi-resolution technique, which yields thirteen wavelet levels or components (the number of wavelet levels is determined by the number of sample data items and the order of wavelet basis). The spectrum obtained from the Fourier analysis of each wavelet component displays a peak, representing the corresponding central frequency, and spreads over a range of frequencies. Figure 3 illustrates the spectrum of wavelet level 9, whose central frequency, identified with the most pronounced peak, corresponds to f_0. Subsequently, the central frequencies of wavelet levels 8, 10, 11 and 12 are given by $f_0/2$, $2f_0$, $4f_0$ and $8f_0$, respectively. This range of frequencies is of major concern in the present investigation; the corresponding central frequencies and their bandwidths are given in table 1. The

https://doi.org/10.1017/S0022112004002319 Published online by Cambridge University Press

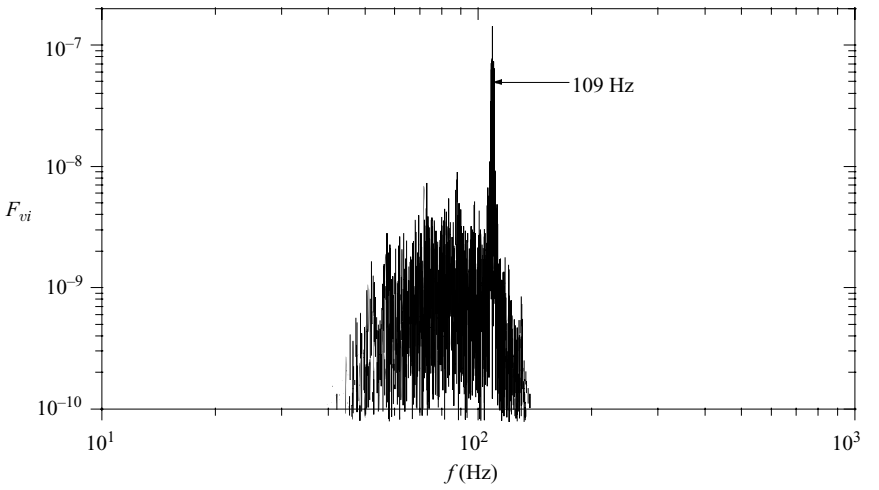


FIGURE 3. Spectra of the wavelet component at f_0 (wavelet level 9) of the v-signal at $y/d \approx 0.7$.

	Wavelet level	Central frequency (Hz)	Frequency bandwidth (Hz)
$f_0/2$	8	55	25–65
f_0	9	109	45–135
$2f_0$	10	218	80–270
$4f_0$	11	436	160–500
$8f_0$	12	872	300–1100

TABLE 1. Central frequencies and bandwidths of wavelet components.

wavelet components of other wavelet levels or central frequencies are not physically important and therefore not discussed.

5. Flow structures of wavelet components

In order to better 'visualize data', sectional streamlines (Perry & Chong 1987), referred to as streamlines for simplicity in the following, were constructed for each wavelet component as well as for measured velocities. The streamlines are viewed in a reference frame translating at the convection velocity of the large-scale structures, which is $U_c = 0.87U_\infty$ (Zhou & Antonia 1992). Figure 4 shows instantaneous streamlines and corresponding normalized vorticity contours, $\omega_z d/U_\infty$ in the (x, y)-plane, where $z/d \approx 0$, and $\omega_y d/U_\infty$ in the (x, z)-plane at $y/d \approx 0.2$ and 0.68, respectively. Streamlines and the $\omega_z d/U_\infty$ contours in the (x, y)-plane at $y/d \approx 0.68$ provide essentially the same information on the flow as those at $y/d \approx 0.2$ and are therefore not shown in figures 4(*e*) and 4(*f*). The solid and broken lines in the vorticity contours represent positive and negative levels, respectively. The same scales are used in the x-, y- and z-directions to avoid the distortion of flow patterns. It is worth pointing out that the finite spacing, about 5 mm, between cross-wires implies a limited spatial resolution in both spanwise and lateral directions, which might subsequently affect the patterns of streamlines and vorticity contours, in particular, those of relatively small-scale structures. Both streamlines (figure 4*a*) and vorticity contours (figure 4*c*) in the (x, y)-plane display the quasi-periodical large-scale organized structures of

https://doi.org/10.1017/S0022112004002319 Published online by Cambridge University Press

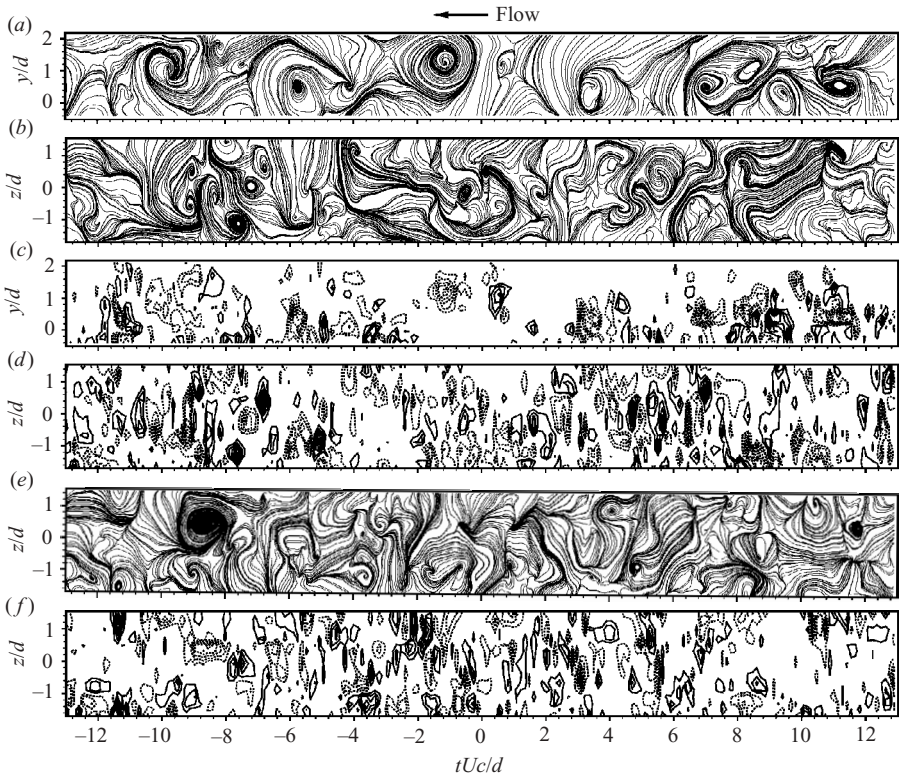


FIGURE 4. Measured instantaneous sectional streamlines: (*a*) in the (x, y)-plane; (*b*) in the (x, z)-plane of $y/d = 0.2$. Vorticity contours: (*c*) $\omega_z d/U_\infty$ in the (x, y)-plane (max: 2.4, min: -2.8, increment: 0.4); (*d*) $\omega_y d/U_\infty$ in the (x, z)-plane of $y/d = 0.2$ (max: 2.4, min: -2.8, increment: 0.4). In the (x, z)-plane of $y/d = 0.68$: (*e*) streamlines; (*f*) $\omega_y d/U_\infty$ (max: 2.8, min: -2.4, increment: 0.4). The contour levels of $|\omega_z|d/U_\infty \leqslant 0.4$ and $|\omega_y|d/U_\infty \leqslant 0.4$ have been removed.

negative vorticity since most of the cross-wires in the (x, y)-plane were placed above the centreline. Organized structures are discernible in the (x, z)-plane. However, it would be difficult to study the behaviours of the structures other than the large-scale ones in either plane.

Figures 5–8 present streamlines and vorticity contours in both planes calculated from the wavelet components of velocity at the central frequencies of f_0, $2f_0$, $4f_0$ and $8f_0$. Different components are identified by their central frequencies, given as a subscript. For example, $(\omega_z)_{f_0}$, $(\omega_z)_{2f_0}$, $(\omega_z)_{4f_0}$ and $(\omega_z)_{8f_0}$ denote the wavelet components of spanwise vorticity for the central frequencies f_0, $2f_0$, $4f_0$ and $8f_0$, respectively. The convection velocity of $U_c = 0.87U_\infty$ for large-scale coherent structures (Zhou & Antonia 1992) was used for the reference frame speed to calculate the streamlines for the wavelet components of f_0 and $2f_0$ and the local mean velocity was used for the other components of higher central frequencies. The flow structure may be characterized by means of critical points, i.e. foci, saddle points and nodes. The points play an important role in the fluid dynamics of a turbulent flow (e.g. Perry & Chong 1987; Zhou & Antonia 1994*a*). In general, the foci of the streamlines coincide with the local vorticity peaks and the saddle points occur between large-scale spanwise vorticity concentrations, suggesting that information on the flow structure

https://doi.org/10.1017/S0022112004002319 Published online by Cambridge University Press

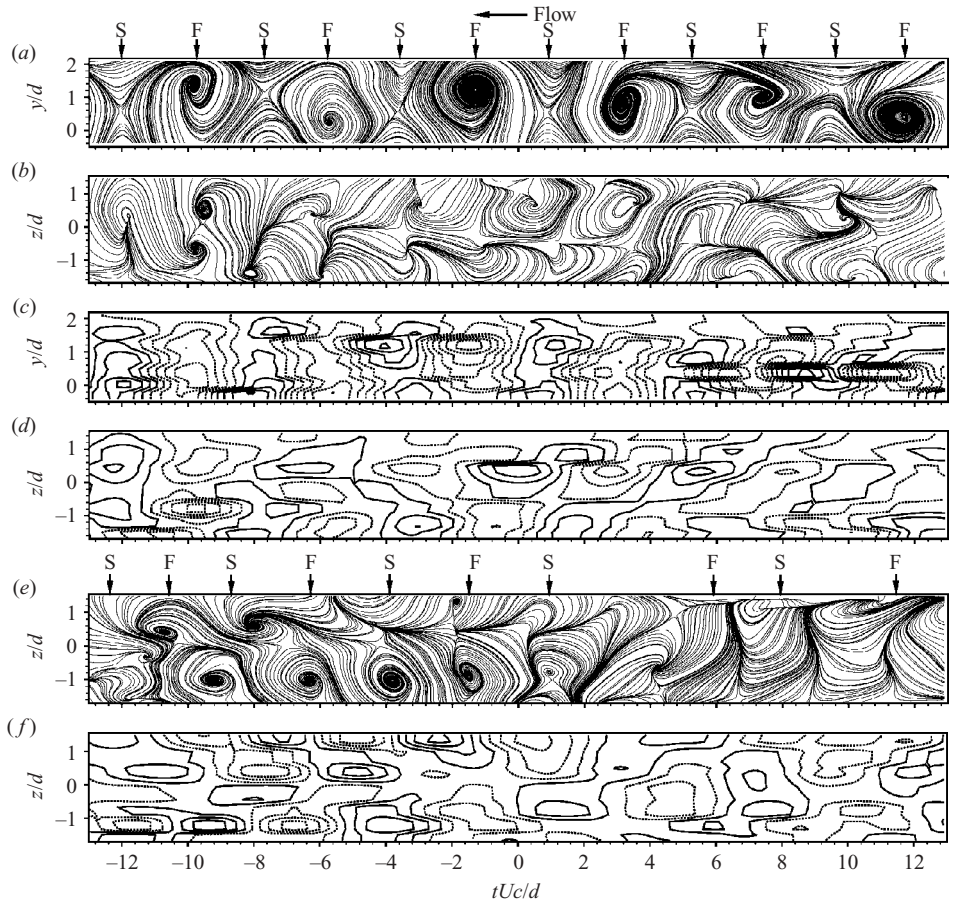


FIGURE 5. Instantaneous sectional streamlines of the wavelet component at f_0: (*a*) in the (x, y)-plane; (*b*) in the (x, z)-plane of $y/d = 0.2$. Vorticity contours: (*c*) $(\omega_z)_{f_0} d/U_\infty$ in the (x, y)-plane (max: 0.45, min: −0.65, Increment: 0.1); (*d*) $(\omega_y)_{f_0} d/U_\infty$ in the (x, z)-plane of $y/d = 0.2$ (max: 0.35, min: −0.35, increment: 0.1). In the (x, z)-plane of $y/d = 0.68$: (*e*) streamlines; (*f*) $(\omega_y)_{f_0} d/U_\infty$ (max: 0.35, min: −0.35, increment: 0.1). The contour levels of $|(\omega_z)_{f_0}| d/U_\infty \leqslant 0.05$ and $|(\omega_y)_{f_0}| d/U_\infty \leqslant 0.05$ have been removed.

can be obtained by examining either streamlines or vorticity. The same comment is applicable for the measured streamlines or vorticity contours (figure 4).

Figure 5 shows streamlines and vorticty contours for the wavelet component at the central frequency f_0. The vortical structures shown in figures 5(*a*) and 5(*c*) have a good correspondence to those in figures 4(*a*) and 4(*c*). The foci and saddle points, whose longitudinal locations are marked by *F* and *S* in figure 5 (also figures 6 and 7), respectively, coincide approximately with those in figure 4(*a*) associated with large-scale structures. However, the structures in figure 5(*a*) appear better organized and exhibit a much stronger periodicity; their topological characteristics and maximum magnitude (0.65) of negative vorticity agree with the conditionally averaged data based on the detections of large-scale vortices (e.g. Zhou & Antonia 1994*a*). It will be seen in § 6 that the corresponding auto or two-point correlation is considerably larger than that of higher central frequencies, consistent with the characteristics of large-scale coherent structures (e.g. Hussain 1986; Robinson 1991). The results

https://doi.org/10.1017/S0022112004002319 Published online by Cambridge University Press

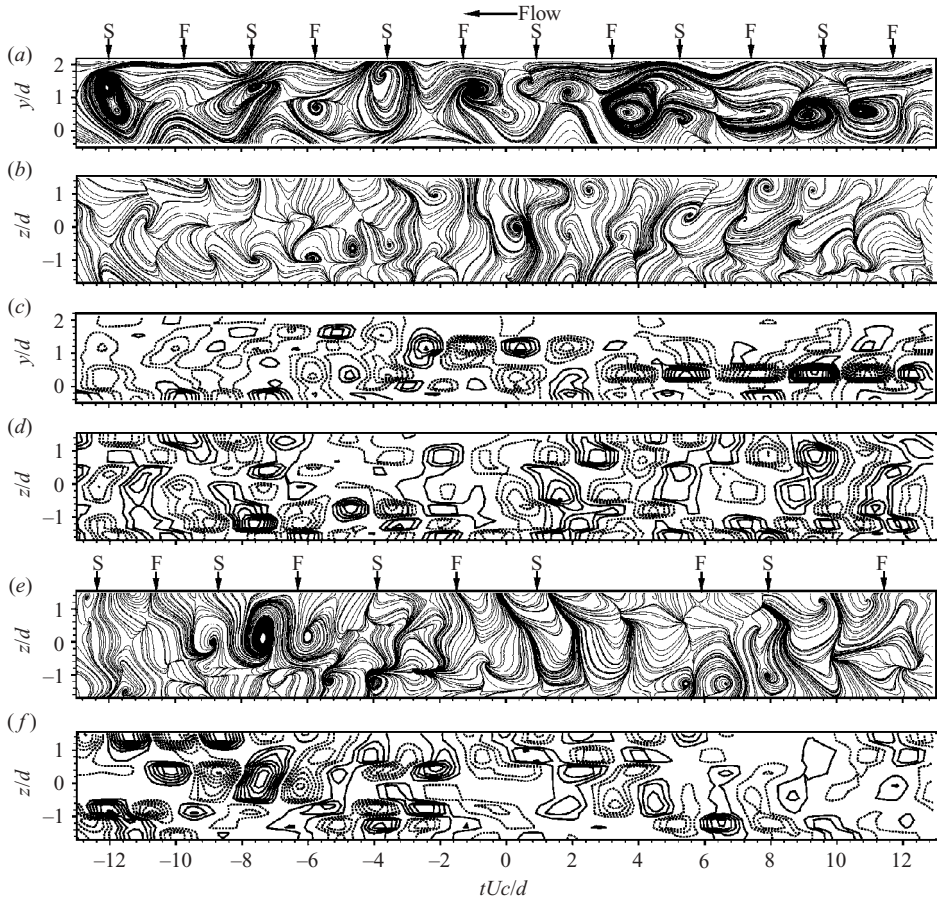


FIGURE 6. Instantaneous sectional streamlines of the wavelet component at $2f_0$: (*a*) in the (x, y)-plane; (*b*) in the (x, z)-plane of $y/d = 0.2$. Vorticity contours: (*c*) $(\omega_z)_{2f_0} d/U_\infty$ in the (x, y)-plane (max: 1.0, min: −1.2, increment: 0.1); (*d*) $(\omega_y)_{2f_0} d/U_\infty$ in the (x, z)-plane of $y/d = 0.2$ (max: 0.7, min: −0.6, increment: 0.1). In the (x, z)-plane of $y/d = 0.68$: (*e*) streamlines; (*f*) $(\omega_y)_{2f_0} d/U_\infty$ (max: 0.7, min: −0.8, increment: 0.1). The contour levels of $|(\omega_z)_{2f_0}| d/U_\infty \leqslant 0.1$ and $|(\omega_y)_{2f_0}| d/U_\infty \leqslant 0.1$ have been removed.

point unequivocally to the wavelet component of f_0 corresponding well to large-scale coherent vortices, indicating the capacity of the present technique to extract large-scale coherent structures from turbulent velocity data and providing a validation for this technique.

A number of other observations can be made from figure 5.

(i) The focus, in general, coincides with the local peak of negative $(\omega_z)_{f_0} d/U_\infty$, while the saddle point occurs at the minimum of $(\omega_z)_{f_0} d/U_\infty$.

(ii) The saddle point is mostly associated with the up–down concentrations of positive vorticity, e.g. at $tU_c/d \approx -8$, -4, 0.8 and 5.2 in figure 5(*c*). The positive vorticity concentration below the saddle point is apparently part of positive-sign vortices, which occur below the centreline, i.e. $y/d < 0$. On the other hand, the vorticity concentration above the saddle point probably results from interactions between two consecutive spanwise structures of negative sign; its positive sign is further consistent with the fact that the vorticity strength of a spanwise vortex is higher than that of the

https://doi.org/10.1017/S0022112004002319 Published online by Cambridge University Press

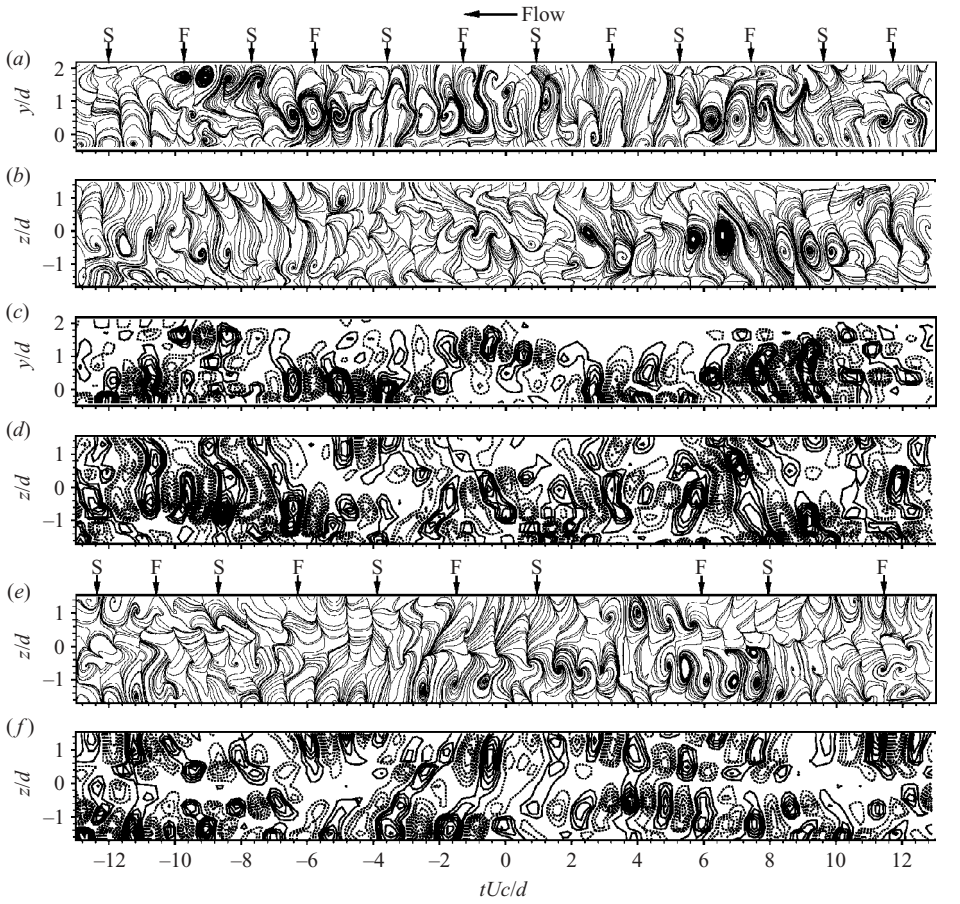


FIGURE 7. Instantaneous sectional streamlines of the wavelet component at $4f_0$: (*a*) in the (x, y)-plane; (*b*) in the (x, z)-plane of $y/d = 0.2$. Vorticity contours: (*c*) $(\omega_z)_{4f_0} d/U_\infty$ in the (x, y)-plane (max: 0.9, min: −1.0, increment: 0.1); (*d*) $(\omega_y)_{4f_0} d/U_\infty$ in the (x, z)-plane of $y/d = 0.2$ (max: 1.1, min: −1.0, increment: 0.1). In the (x, z)-plane of $y/d = 0.68$: (*e*) streamlines; (*f*) $(\omega_y)_{4f_0} d/U_\infty$ (max: 1.1, min: −1.0, increment: 0.1). The contour levels of $|(\omega_z)_{4f_0}| d/U_\infty \leqslant 0.1$ and $|(\omega_y)_{4f_0}| d/U_\infty \leqslant 0.1$ have been removed.

neighbouring downstream one because of a fast decay in the vortex strength as x/d increases (Zhou & Antonia 1993). This secondary structure of positive vorticity (or negative-sign vorticity if below the centreline) has not been observed from previous conditional data, e.g. Hussain & Hayakawa (1987) and Zhou & Antonia (1994*a*), probably as a result of positive and negative vorticity cancellation in conditional averaging, which is caused by lateral jittering in the location of saddle points. For instance, one saddle point at $tU_c/d \approx 0.9$ occurs at $y/d \approx 0.5$, while another saddle point at $tU_c/d \approx 9.5$ appears at $y/d \approx 1$. If the flow field is conditionally averaged based on saddle points, such as Zhou & Antonia (1994*a*, *b*) did, the positive spanwise vorticity concentration above the former will be at least partially cancelled by the negative spanwise vorticity around the latter.

(iii) The vorticity concentrations are evident in the (x, z)-plane and may correspond spatially to foci or saddle points in the (x, y)-plane. Previous work on turbulent near-wakes revealed two main types of vertical structure that contribute to the

https://doi.org/10.1017/S0022112004002319 Published online by Cambridge University Press

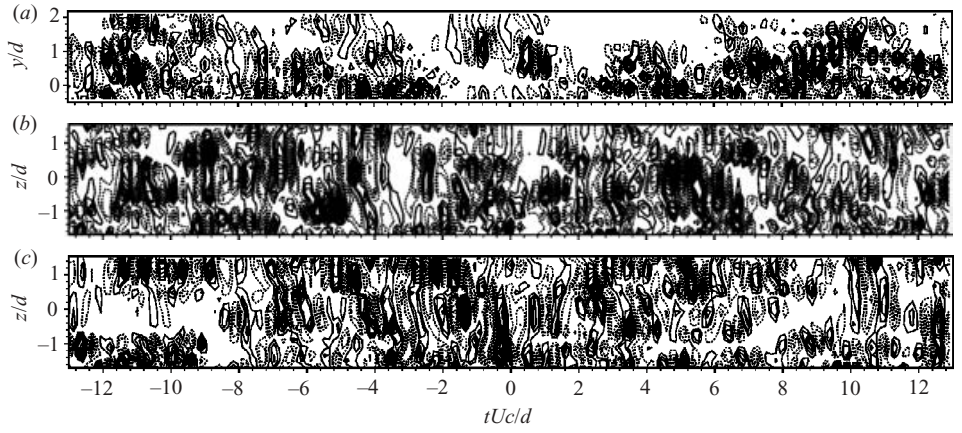


FIGURE 8. Vorticity contours of the wavelet component at $8f_0$: (*a*) $(\omega_z)_{8f_0}d/U_\infty$ in the (x, y)-plane (max: 1.2, min: −1.1, increment: 0.1); (*b*) $(\omega_y)_{8f_0}d/U_\infty$ in the (x, z)-plane of $y/d = 0.2$ (max: 1.7, min: −1.8, increment: 0.1); (*c*) $(\omega_y)_{8f_0}d/U_\infty$ in the (x, z)-plane of $y/d = 0.68$ (max: 1.1, min: −1.0, increment: 0.1). The contour levels of $|(\omega_z)_{8f_0}|d/U_\infty \leqslant 0.1$ and $|(\omega_y)_{8f_0}|d/U_\infty \leqslant 0.1$ have been removed.

three-dimensionality of flow. One is quasi-two-dimensional spanwise structure with predominantly spanwise vorticity. The other generally lies in the (x, y)-plane and has vorticity components in the x and y directions only. It has been suggested that the latter structures are in the form of ribs, which are inclined in the (x, y)-plane and either wrap around or connect cross-stream spanwise rib structures (e.g. Zhang *et al.* 2000). If ribs are indeed inclined in the (x, y)-plane, they should intersect the (x, z)-plane between successive spanwise structures. Although the presence of rib structures has been documented in the near wake (e.g. Hussain & Hayakawa 1987; Zhou & Antonia 1994*a*), many of their details are not clarified. Presumably, the concentrations of transverse vorticity corresponding to the foci in the (x, y)-plane originate from the three-dimensionality of spanwise structures. On the other hand, those corresponding to the saddle points are probably the signatures of rib structures. If so, a number of remarks can be made on rib structures. (i) The rib structure is appreciably smaller in size than the spanwise structure, but they are of the same order of magnitude. (ii) Hussain & Hayakawa (1987) proposed that the positive and negative rib structures occurred alternately in the spanwise direction and that the rib structures of opposite sign should occur alternately in the streamwise direction. Indeed, the rib structures tend to show alternate occurrence of opposite sign in the spanwise direction, e.g. at $tU_c/d \approx -3.5$, 5.3 and 9.5 in figure 5*d* and −8.5 and 1 in figure 5(*f*). In the streamwise direction, the vorticity concentrations of opposite sign in the (x, z)-plane do show alternate occurrence; for example, those structures occur at $z/d \approx 0.5$ in figure 5(*d*) and at $z/d = -1$ in figure 5(*f*). However, some of these structures correspond to foci in the (x, y)-plane and may not be classified as rib structures. It is not evident that the rib structures of opposite sign occur alternately in the streamwise direction. (iii) The spanwise spacing of rib structures is of the order of $1d$, as illustrated at $tU_c/d \approx -7$, −3, 1, 5.5 and 10.5 in the (x, z)-plane of $y/d \approx 0.2$ (figures 5*b* and 5*c*). Previous work (Mansy, Yang & Williams 1994; Zhang *et al.* 1995; Williamson 1996*b*; Henderson 1997) at small Reynolds numbers has suggested that there are two modes of streamwise structures. Mode A is of relatively large scale with a spanwise wavelength of about $4d$. Mode B has a significantly finer scale and a

https://doi.org/10.1017/S0022112004002319 Published online by Cambridge University Press

spanwise wavelength of $1d$. The latter was observed by Chyu & Rockwell (1996) using particle image velocimetry at $Re = 10 \times 10^3$. The present data tend to show a spanwise wavelength of $1d$ for rib structures, suggesting the occurrence of mode B structures. This is probably because the eight cross-wires aligned in the (x, z)-plane only covered a spanwise extent of about $3d$, making it difficult to capture the characteristics of mode A structures.

(iv) The contours of lateral vorticity, $(\omega_y)_{f_0} d/U_\infty$, at $y/d \approx 0.2$ (figure 5*d*) appear qualitatively the same as those at $y/d \approx 0.68$ (figure 5*f*). However, streamlines in the (x, z)-plane (figures 5*b* and 5*e*) indicate that the lateral vortical structures occur more frequently at $y/d \approx 0.68$ than at $y/d \approx 0.2$. As a matter of fact, those vortical structures in figure 5(*e*) display a quasi-periodicity for $tU_c/d \approx -9 \sim 1$, and furthermore tend to correspond to either foci or saddle points, suggesting that the three-dimensionality of spanwise vortices and quasi-longitudinal rib structures are probably responsible for these transverse structures. The observation is reasonable since spanwise vortices occur most probably at $y/d \approx 0.7$ (Hussain & Hayakawa 1987). On the other hand, the rib structures occur near the saddle point, which is, in general, further away from the centreline, compared with the spanwise vortex centre (Zhou & Antonia 1994*a*), that is, the rib structure could be closer to $y/d \approx 0.68$ than $y/d \approx 0.2$. Note that the transverse structures may be absent, e.g. at $tU_c/d \approx 2 \sim 12$.

(v) The maximum magnitude of vorticity in the (x, z)-plane is 0.35 (negative), approximately half of the 0.65 in the (x, y)-plane. The spanwise structures are the primary structures in the near wake and those in the (x, z)-plane are the secondary structures, which largely result from the three-dimensionality of the spanwise structures or rib structures. Therefore, large-scale vorticity associated with these relatively large-scale structures is stronger in the (x, y)-plane than in the (x, z)-plane. However, the maximum magnitude of vorticity, approximated from the measured velocity, in the (x, z)-plane (figure 4*d*) is 2.8, about the same as that in the (x, y)-plane (figure 4*c*). It will be seen from components at the central frequency $\geqslant 4f_0$ that relatively small-scale vorticity in the (x, z)-plane has a higher concentration than that in the (x, y)-plane. This will be discussed later in more details.

As the central frequency increases to $2f_0$, the spanwise vortical structures in the (x, y)-plane (figure 6*a*) mostly correspond in location to either foci or saddle points, marked by 'F' and 'S', respectively, which are associated with large-scale spanwise structures and identified from the streamlines of the wavelet component at f_0. Those corresponding to 'S', for example, at $tU_c/d \approx -12$, -3.8 and -7.6 tend to occur above the saddle points, internally consistent with the secondary spanwise structures observed from the contours of $(\omega_z)_{f_0} d/U_\infty$ (figure 5*c*). Streamlines (figure 6*b*) in the (x, z)-plane show a different flow structure from that (figure 6*a*) in the (x, y)-plane. The vorticity strength in both planes almost doubles that at the central frequency of f_0. Nonetheless, this strength is still significantly weaker in the (x, z)-plane than in the (x, y)-plane, the maximum contour level of $(\omega_y)_{2f_0} d/U_\infty$ (figure 6*d*) being 0.7, significantly smaller than that the 1.2 of $(\omega_z)_{2f_0} d/U_\infty$. The difference suggests that the structures in the (x, y)-plane are connected to primary or secondary spanwise structures, while those in the (x, z)-plane result from the three-dimensionality of primary spanwise structures and rib structures. Furthermore, the vorticity concentrations of opposite sign tend to occur alternately in the longitudinal direction, irrespective of the (x, y) or (x, z)-plane. The alternate occurrence of opposite-sign vorticity concentrations, mostly associated with the saddle points, is also observed in the spanwise direction, for example, at $tU_c/d \approx -7.5$, 5 and 9.6 in figure 6(*d*) ($y/d \approx 0.2$) and at $tU_c/d \approx -8.8$ and -4 in figure 6(*f*) ($y/d \approx 0.68$). The spanwise spacing between these

https://doi.org/10.1017/S0022112004002319 Published online by Cambridge University Press

concentrations is of the order of $1d$. The observation is again linked to the behaviour of the rib structures.

Once the central frequency reaches $4f_0$, the structures of smaller scale appear all over the flow. The streamlines (figures 7*a*, 7*b* and 7*e*) show turbulent structures, not so distinct albeit discernible, between the two planes as the wavelets components of f_0 (figure 5) and $2f_0$ (figure 6). The vorticity concentrations (figures 7*c* and 7*d*) tend to be arranged alternately in sign along the flow direction in both planes. However, there does not seem to be any correlation between vorticity concentrations and the location of foci or saddle points. Furthermore, the transverse vorticity concentrations (figures 7*d* and 7*f*) in the (x, z)-plane appear stretched in the spanwise direction, showing a very different pattern from those at the central frequencies of f_0 and $2f_0$. The maximum strength of spanwise vorticity (figure 7*c*) in the (x, y)-plane decreases slightly for both signs, down from 1.2 at $2f_0$ to 1.0 at $4f_0$ for negative sign, but the maximum transverse vorticity (figure 7*c*) in the (x, z)-plane increases from 0.7 at $2f_0$ (figure 6*d*) to about 1.1 at $4f_0$. The observation conforms to the conception that the spanwise structures are largely associated with large-scale vorticity, while the transverse structures are dominated by relatively small-scale vorticity. Subsequently, the vorticity strength in the (x, z)-plane now exceeds that in the (x, y)-plane. In summary, for the wavelet components of $4f_0$ and probably higher central frequencies it seems difficult to distinguish the turbulent structures in either plane associated with the large-scale spanwise structures from those associated with the rib structures. Perhaps, the turbulent structures are not so well 'organized' any more and predominantly incoherent.

At the central frequency of $8f_0$, vorticity concentrations (figure 8) appear in strips, running spanwise, irrespective of the (x, y)- or (x, z)-plane. (Streamlines were not constructed for the wavelet components of central frequencies higher than $4f_0$.) Again, their occurrence in the (x, y)- and (x, z)-plane seems totally decoupled from the existence of foci or saddle points. The vorticity strength in the (x, y)-plane is almost unchanged, compared with that of $4f_0$, for negative sign, but increases appreciably for the positive sign, from $(\omega_z)_{4f_0}d/U_\infty = 0.9$ to $(\omega_z)_{8f_0}d/U_\infty = 1.2$. The result is internally consistent with earlier observation (figure 5*c*) that the negative-sign vorticity is associated with large-scale spanwise structures, and the positive-sign vorticity occurs mostly in the saddle region and is associated with relatively small-scale structures. Meanwhile, the increase in the vorticity strength in the (x, z)-plane, compared with that of $4f_0$, is particularly evident (figures 8*b* and 8*c*), up to 50%, resulting in a maximum $(\omega_y)_{8f_0}d/U_\infty$ 50% larger than that of $(\omega_z)_{8f_0}d/U_\infty$.

6. Scales of wavelet components

6.1. *Lateral scales*

To estimate the lateral extent of the turbulent structures of different scales, the correlation coefficient of the wavelet component, $R_{\alpha\alpha i}$, of the ith component in the (x, y)-plane is defined as

$$R_{\alpha\alpha i} = \frac{\overline{\alpha_{i0}\alpha_i}}{\left(\overline{\alpha_{i0}^2}\,\overline{\alpha_i^2}\right)^{1/2}}. \tag{13}$$

In (13), α may represent u or v, the subscripts $i0$ and i denote the reference signal, obtained from a cross-wire in the (x, y)-plane at $y/d \approx 0.7$, and a signal from another cross-wire in the same plane, respectively.

https://doi.org/10.1017/S0022112004002319 Published online by Cambridge University Press

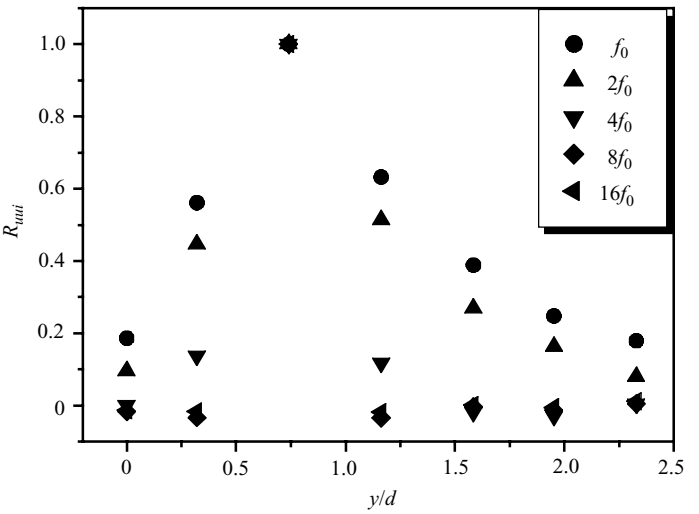


FIGURE 9. Lateral two-point velocity correlation coefficients of the wavelet components at various central frequencies (the reference u is at $y/d \approx 0.7$).

Figure 9 presents the lateral variation of R_{uui} for different central frequencies. R_{uui} is unity at $y/d \approx 0.7$ and decreases as u_i moves away from the reference signal. As the central frequency increases, R_{uui} reduces since the higher central frequency corresponds to the smaller scales of structures. The decrease from f_0 to $2f_0$ is small, suggesting that the scale of turbulent structures is comparable between the two central frequencies. However, R_{uui} experiences a sharp fall from $2f_0$ to $4f_0$. For example, R_{uui} at $y/d \approx 1.2$ (about $0.4d$ away from the reference signal) drops from about 0.5 to 0.1, and further slides to almost zero at $8f_0$. It may be concluded that the flow structures corresponding to the wavelet components of f_0 and $2f_0$ are characterized by a lateral scale significantly larger than those of higher central frequencies, and those at and beyond $8f_0$ could be considered to be incoherent.

6.2. *Spanwise scales*

The spanwise scale of wavelet components may be examined using two-point u-correlation in the spanwise direction. The correlation coefficient of the wavelet component between u_i from cross-wires in the (x, z)-plane and u_{z0i} from the cross-wire in the (x, y)-plane, which is closest to the (x, z)-plane, may be defined as

$$R_{u_0ui} = \frac{\overline{u_{z0i} u_i}}{\left(\overline{u_{z0i}^2}\,\overline{u_i^2}\right)^{1/2}}. \tag{14}$$

This coefficient provides a measure of the two-dimensionality of wavelet components. Figure 10 shows the spanwise variation of R_{u_0ui} in the (x, z)-plane at $y/d \approx 0.68$. The correlation coefficient is unity at $z/d = 0$, i.e. in the (x, y)-plane, and diminishes as z/d increases in magnitude. Evidently, R_{u_0ui} decreases as the central frequency increases since the larger-scale structures are expected to be more 'two-dimensional' than those smaller-scale structures. In similarity to the lateral scales of wavelet components (figure 9), the correlation coefficient corresponding to f_0 or $2f_0$ is considerably larger than that of higher central frequencies, implying that the corresponding structures are much more two-dimensional, as expected. As observed earlier, the wavelet component of f_0 corresponds well to the large-scale spanwise structures, which are

https://doi.org/10.1017/S0022112004002319 Published online by Cambridge University Press

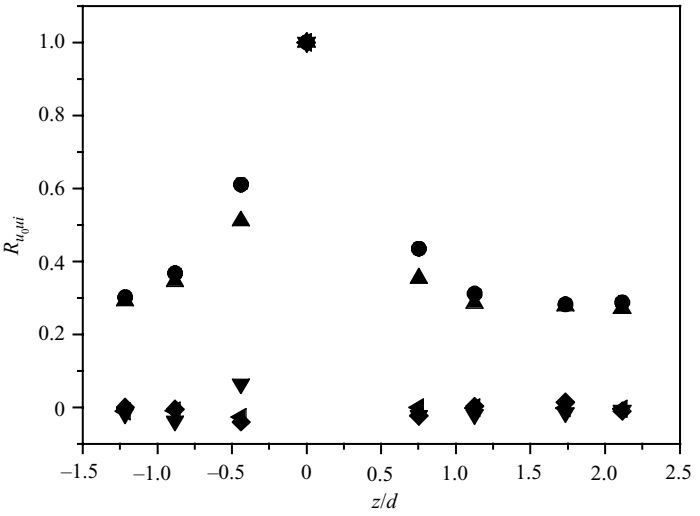


FIGURE 10. Spanwise variation of the two point velocity correlation coefficient, $R_{u_0ui} = \overline{u_{z0i} u_i} / (\overline{u_{z0i}^2}\,\overline{u_i^2})^{1/2}$, of the wavelet components in the (x, z)-plane of $y/d = 0.68$ at various central frequencies (the reference u is in the (x, y)-plane. The symbols are as in figure 9.

shed from the cylinder in 'rolls'. The structures as represented by the wavelet component of $2f_0$ possibly result from vigorous interactions between the large-scale spanwise structures and may thus inherit two-dimensionality from those of f_0. It is worth commenting that for the same z/d, R_{u_0ui} at $y/d \approx 0.68$ is appreciably larger than that at $y/d \approx 0.2$ (not shown here), apparently because $y/d \approx 0.68$ is the most probable lateral location of vortices.

6.3. *Longitudinal scales*

The longitudinal scales of wavelet components may be indicated by the wavelet multi-resolution auto-correlation coefficient (Li 1998), namely

$$R_{\alpha i}(\tau) = \frac{\lim\limits_{T\to\infty} \dfrac{1}{T} \displaystyle\int_{-T/2}^{T/2} \alpha_i(t)\alpha_i(t+\tau)\,\mathrm{d}t}{\lim\limits_{T\to\infty} \dfrac{1}{T} \displaystyle\int_{-T/2}^{T/2} \alpha_i^2(t)\,\mathrm{d}t}. \tag{15}$$

As expected, R_{ui} (figure 11) at $\tau U_c/d = 0$ drops faster for a higher central frequency. This is particularly evident when the central frequency is above $2f_0$. As a matter of fact, R_{ui} at f_0 and $2f_0$ displays a quasi-periodical wave as $\tau U_c/d$ increases, suggesting a link between the wavelet components of f_0 and $2f_0$ and the quasi-periodical large-scale spanwise structures in this flow. R_{ui} at $4f_0$ also shows oscillation, which decays quickly. For a central frequency higher than $4f_0$, R_{ui} approaches essentially zero at $\tau U_c/d \approx 1$ or much sooner.

In summary, the two-point correlation and auto-correlation coefficients all point to the wavelet components of f_0 and $2f_0$ being characterized by the turbulent structures of scales distinctly larger than those of higher central frequencies, indicating the predominance of large-scale spanwise coherent structures and perhaps also including intermediate-scale coherent structures such as the longitudinal rib-like structures. While the wavelet component of $4f_0$ retains a relatively week coherence, those of

https://doi.org/10.1017/S0022112004002319 Published online by Cambridge University Press

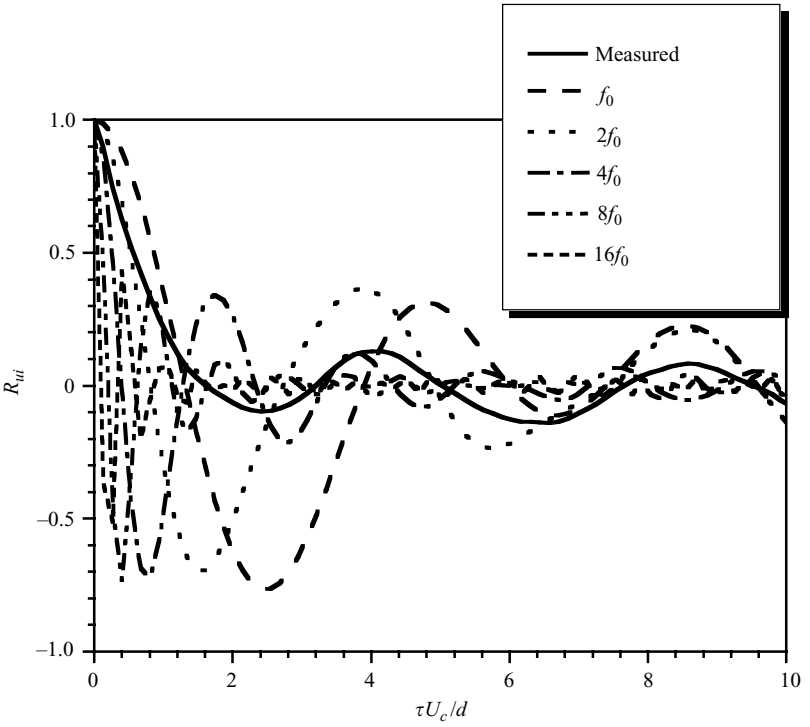


FIGURE 11. Auto-correlation coefficients of the measured velocity signals at $y/d \approx 0.7$ and their wavelet components at various central frequencies.

higher central frequencies do not show coherence, exhibiting the characteristics of incoherent structures.

7. Probability density function of wavelet components

Figure 12 presents the probability density functions, P, of wavelet components v_i along with the measured v signal at $y/d \approx 0.7$ in the (x, y)-plane. For the v signal, P (figure 12*a*) displays considerable spread, ranging from -2.5 to $2.5\,\mathrm{m\,s^{-1}}$, and asymmetrical with respect to $v = 0$, showing a noticeable departure from the Gaussian distribution. In the case of wavelet components, however, P is significantly less asymmetrical with respect to $v = 0$, irrespective of central frequencies, and appears more like a Gaussian distribution. P at f_0 (figure 12*b*) and $2f_0$ (figure 12*c*) spreads more on both sides, implying a larger fluctuating lateral velocity. The spread shrinks for increasing central frequencies, indicating a reducing fluctuation within a wavelet component. Correspondingly, the peak of P increases as the central frequency increases.

8. Conclusions

The wavelet multi-resolution technique, based on an orthogonal wavelet transform, has been applied to analysing experimental velocity data obtained simultaneously in two orthogonal planes in the turbulent near wake of a circular cylinder. Using this technique, the turbulent flow is decomposed into a number of wavelet components based on their central frequencies. The wavelet component at a central frequency

https://doi.org/10.1017/S0022112004002319 Published online by Cambridge University Press

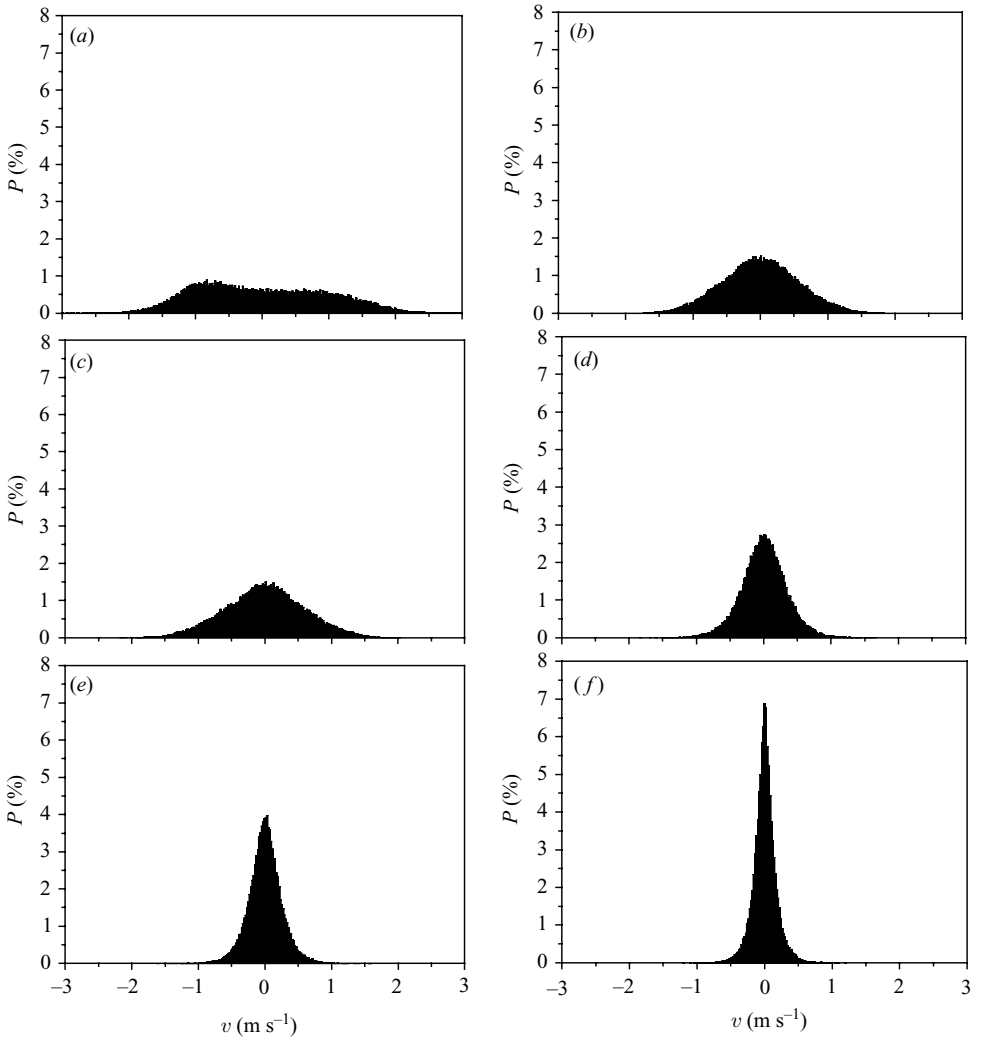


FIGURE 12. Probability density functions of the measured and the wavelet components at various central frequencies at $y/d = 0.7$. (*a*) Measured; (*b*) f_0; (*c*) $2f_0$; (*d*) $4f_0$; (*e*) $8f_0$; (*f*) $16f_0$.

identical to the dominant vortex frequency exhibits the characteristics of the Kármán vortices, indicating the capacity of the present technique to extract large-scale coherent structures.

The spanwise vorticity contours of the wavelet component at f_0 display a secondary spanwise structure above the saddle point, whose vorticity is opposite-signed to that of the spanwise structures. This structure is observed for the first time and probably results from the strong interactions between the consecutive spanwise structures of the same sign. Its occurrence and vorticity sign is consistent with the streamwise decay in the vorticity strength of the spanwise structures.

The correspondence between the central frequencies and spatial scales of the wavelet components is examined based on the two-point velocity correlation along the y- and z-directions and the auto-correlation coefficient (the x-direction). The u- or v-correlation coefficient for the wavelet components of f_0 and $2f_0$ is large over

https://doi.org/10.1017/S0022112004002319 Published online by Cambridge University Press

a significant distance in both x- and y-directions, demonstrating the feature of large scales. Furthermore, the u-correlation coefficient of the wavelet component at f_0 or $2f_0$ exceeds 0.5 over about $1d$ in the spanwise direction, displaying appreciable two-dimensionality. The results point to the two wavelet components being connected to the spanwise structures of large scales and perhaps intermediate scales. The wavelet components of $4f_0$ display much smaller correlation, though still appreciable, in the x- or y-direction than those of f_0 or $2f_0$, and the corresponding spanwise u-correlation coefficient quickly drops to zero, indicating highly three-dimensional characteristics. The wavelet components at $8f_0$ and higher, lose coherence very quickly.

The experiments were conducted at Professor R. A. Antonia's laboratory at The University of Newcastle with financial support from the Australian Research Council. A. R. wishes to acknowledge support given to him by Grant-in-Aid for Scientific Research (C) (no. 13650189) from the Japanese Society for the Promotion of Science. Y. Z. wishes to acknowledge support by the Research Grants Council of the Government of the HKSAR through Grants PolyU 5316/03E and by the Central Research Grant of The Hong Kong Polytechnic University through Grant G-YD21.

REFERENCES

Argoul, F., Arneodo, A., Grasseau, G., Gagne, Y., Hopfinger, E. J. & Frisch, U. 1989 Wavelet analysis of turbulence reveals the multifractal nature of the Richardson cascade. *Nature* **338**, 51–53.

Bonnet, J. P., Delville, J., Glauser, M. N., Antonia, R. A., Bisset, D. K., Cole, D. R., Fiedler, H. E., Garem, J. H., Hilberg, D., Jeong, J., Kevlahan, N. K. R., Ukeiley, L. S. & Vincendeau, E. 1998 Collaborative testing of eddy structure identification methods in free turbulent shear flows. *Exps. Fluids* **25**, 197–225.

Brede, M., Eckelmann, H. & Rockwell, D. 1996 On secondary vortices in the cylinder wake. *Phys. Fluids* **8**, 2117–2124.

Cantwell, B. & Coles, D. 1983 An experimental study of entrainment and transport in the turbulent near wake of a circular cylinder. *J. Fluid Mech.* **136**, 321–374.

Chyu, C. & Rockwell, D. 1996 Evolution of patterns of streamwise vorticity in the turbulent near wake of a circular cylinder. *J. Fluid Mech.* **320**, 117–137.

Daubechies, I. 1992 *Ten Lectures on Wavelets*. Society for Industrial and Applied Mathematics.

De Souza, F., Delville, J., Lewalle, J. & Bonnet, J. P. 1999 Large scale coherent structures in a turbulent boundary layer interacting with a cylinder wake. *Exp. Thermal Fluid Sci.* **19**, 204–213.

Farge, M. 1992 Wavelet transforms and their applications to turbulence. *Annu. Rev. Fluid Mech.* **24**, 395–457.

Farge, M., Schneider, K. & Kevlahan, N. 1999 Non-Gaussianity and coherent vortex simulation for two-dimensional turbulence using an adaptive orthogonal wavelet basis. *Phys. Fluids* **11**, 2187–2201.

Ferre, J. A. & Giralt, F. 1989 Pattern-recognition analysis of the velocity field in plane turbulent wakes. *J. Fluid Mech.* **198**, 27–64.

Henderson, R. D. 1997 Nonlinear dynamics and pattern formation in turbulent wake transition. *J. Fluid Mech.* **352**, 65–112.

Higuchi, H., Lewalle, J. & Crane, P. 1994 On the structure of a two-dimension wake behind a pair of flat plates. *Phys. Fluids* **6**, 297–305.

Hussain, A. K. M. F. 1986 Coherent structures and turbulence. *J. Fluid Mech.* **173**, 303–356.

Hussain, A. K. M. F. & Hayakawa, M. 1987 Education of large-scale organized structures in a turbulent plane wake. *J. Fluid Mech.* **180**, 193–229.

Kiya, M. & Matsumura, M. 1988 Incoherent turbulence structure in the near wake of a normal Plate. *J. Fluid Mech.* **190**, 343–356.

https://doi.org/10.1017/S0022112004002319 Published online by Cambridge University Press

Li, H. 1998 Identification of coherent structure in turbulent shear flow with wavelet correlation analysis. *Trans. ASME* I: *J. Fluids Engng* **120**, 778–785.

Li, H. & Nozaki, T. 1995 Wavelet analysis for the plane turbulent jet (analysis of large eddy structure). *JSME Intl J. Fluids Thermal Engng* **38**, 525–531.

Liandrat, J. & Moret-Bailly, F. 1990 The wavelet transform: some applications to fluid dynamics and turbulence. *Eur. J. Mech.* B/*Fluids* **9**, 1–19.

Lin, J.-C., Vorobieff, P. & Rockwell, D. 1996 Space–time imaging of a turbulent nar-wake by high-image-density particle image cinematography. *Phys. Fluids* **8**, 555–564.

Mallat, S. 1989 A theory for multi-resolution signal decomposition: the wavelet representation. *IEEE Trans. PAMI* **11**, 674–693.

Mansy, H., Yang, P. & Williams, D. R. 1994 Quantitative measurements of three-dimensional structures in the wake of a circular cylinder. *J. Fluid Mech.* **270**, 277–296.

Meneveau, C. 1991 Analysis of turbulence in the orthonormal wavelet representation. *J. Fluid Mech.* **232**, 469–520.

Mi, J. & Antonia, R. A. 1996 Vorticity characteristics of the turbulent intermediate wake. *Exps. Fluids* **20**, 383–392.

Mouri, H., Kubotani, H., Fujitani, T., Niino, H. & Takaoka, M. 1999 Wavelet analysis of velocities in laboratory isotropic turbulence. *J. Fluid Mech.* **389**, 229–254.

Perry, A. E. & Chong, M. S. 1987 A description of eddy motions and flow patterns using critical-point concepts. *Annu. Rev. Fluid Mech.* **19**, 125–155.

Robinson, S. K. 1991 Coherent motions in the turbulent boundary layer. *Annu. Rev. Fluid Mech.* **23**, 601–639.

Wei, T. & Smith, C. R. 1986 Secondary vortices in the wake of circular cylinders. *J. Fluid Mech.* **169**, 513–533.

Williamson, C. H. K. 1996*a* Vortex dynamics in the cylinder wake. *Annu. Rev. Fluid. Mech.* **28**, 477–539.

Williamson, C. H. K. 1996*b* Three-dimensional wake transition. *J. Fluid Mech.* **328**, 345–407.

Wu, J., Sheridan, J., Welsh, M. C. & Hourigan, K. 1996 Three-dimensional vortex structures in a cylinder wake. *J. Fluid Mech.* **312**, 201–222.

Zhang, H. J., Zhou, Y. & Antonia, R. A. 2000 Longitudinal and spanwise structures in a turbulent wake. *Phys. Fluids* **12**, 2954–2964.

Zhang, H.-Q., Fey, U., Noack, B. R., König, M. & Eckelmann, H. 1995 On the transition of the cylinder wake. *Phys. Fluids* **7**, 779–794.

Zhou, Y. & Antonia, R. A. 1992 Convection velocity measurements in a cylinder wake. *Exps Fluids* **13**, 63–70.

Zhou, Y. & Antonia, R. A. 1993 A study of turbulent vortices in the wake of a cylinder. *J. Fluid Mech.* **253**, 643–661.

Zhou, Y. & Antonia, R. A. 1994*a* Critical points in a turbulent near-wake. *J. Fluid Mech.* **275**, 59–81.

Zhou, Y. & Antonia, R. A. 1994*b* Effect of initial conditions on structures in a turbulent near-wake. *AIAA J.* **32**, 1207–1213.

Zhou, Y., Zhang, H. J. & Yiu, M. W. 2002 The turbulent wake of two side-by-side circular cylinders. *J. Fluid Mech.* **458**, 303–332.

https://doi.org/10.1017/S0022112004002319 Published online by Cambridge University Press